AIP Advances

Modification of magnetocrystalline anisotropy via ion-implantation

Cite as: AIP Advances **10**, 045306 (2020); https://doi.org/10.1063/1.5134867
Submitted: 02 November 2019 . Accepted: 11 March 2020 . Published Online: 01 April 2020

Michael S. Lee, Rajesh V. Chopdekar, Padraic Shafer, Elke Arenholz, and Yayoi Takamura

COLLECTIONS

This paper was selected as an Editor's Pick

View Online Export Citation CrossMark

© 2020 Author(s).

Modification of magnetocrystalline anisotropy via ion-implantation

Cite as: AIP Advances 10, 045306 (2020); doi: 10.1063/1.5134867
Submitted: 2 November 2019 • Accepted: 11 March 2020 •
Published Online: 1 April 2020

View Online Export Citation CrossMark

Michael S. Lee,[1] Rajesh V. Chopdekar,[1,2] Padraic Shafer,[2] Elke Arenholz,[2,3] and Yayoi Takamura[1,a)]

AFFILIATIONS

[1] Department of Materials Science and Engineering, University of California, Davis, Davis, California 95616, USA
[2] Advanced Light Source, Lawrence Berkeley National Laboratory, Berkeley, California 94720, USA
[3] Cornell High Energy Synchrotron Source, Cornell University, Ithaca, New York 14853, USA

[a)] **Author to whom correspondence should be addressed:** ytakamura@ucdavis.edu

ABSTRACT

The ability to systematically modify the magnetic properties of epitaxial $La_{0.7}Sr_{0.3}MnO_3$ thin films is demonstrated through the use of Ar^+ ion implantation. With increasing implant dose, a uniaxial expansion of the *c*-axis of the unit cell leads to a transition from in-plane toward perpendicular magnetic anisotropy. Above a critical dose of 3×10^{13} Ar^+/cm^2, significant crystalline disorder exists leading to a decrease in the average Mn valence state and near complete suppression of magnetization. Combined with lithographic techniques, ion implantation enables the fabrication of magnetic spin textures consisting of adjacent regions with tunable magnetic anisotropy in complex oxide thin films.

© 2020 Author(s). All article content, except where otherwise noted, is licensed under a Creative Commons Attribution (CC BY) license (http://creativecommons.org/licenses/by/4.0/). https://doi.org/10.1063/1.5134867

Fine control of magnetocrystalline anisotropy is critical for improvements in technologies dependent on magnetic thin films with perpendicular magnetic anisotropy (PMA), such as hard disk drives, and will be necessary for future magnetic devices based on spin textures.[1–3] Artificial magnetic skyrmions are one such example, but their fabrication can require lithographically defined, multilayer structures to form adjacent regions of both in-plane and out-of-plane moments.[4–8] The ability to modulate magnetocrystalline anisotropy within a single film would streamline device processing and minimize the complexity of introducing additional interfaces. Transition metal oxides (TMOs) are well suited to that end as the magnetocrystalline anisotropy can be tuned through multiple pathways such as chemical doping,[9] interfacial interactions,[10] and lattice distortions.[11] Earlier work highlighted the relationship between the magnetic easy axis in TMOs [e.g., $La_{0.7}Sr_{0.3}MnO_3$ (LSMO)[12] and $La_{1-x}Sr_xCoO_3$[13]] and epitaxial strain. When LSMO is grown under tensile or slightly compressive strain on $SrTiO_3$ [STO, ratio of *c*- to *a*-lattice parameters (*c*/*a* ratio) = 0.987] or $(LaAlO_3)_{0.3}(Sr_2TaAlO_6)_{0.7}$ (LSAT, *c*/*a* ratio = 1.007) substrates, respectively, the magnetic moments prefer to lie within the film plane but switch to out-of-plane under large compressive strain imposed by $LaAlO_3$ (LAO, *c*/*a* ratio = 1.053).[12,13] More recently, the anisotropy of $La_{1-x}Sr_xMnO_3$ was shown to be highly tunable in superlattices with $SrIrO_3$ with PMA emerging for $x > 0.5$.[10] These studies demonstrate the potential for designing the magnetocrystalline anisotropy but require specific interfaces or substrate selection that cannot be readily modified on the scale of magnetic device features. Ion irradiation of silicon single crystals,[14] yttria-stabilized zirconia (YSZ),[15] and epitaxial TMO films[16,17] was demonstrated to induce uniaxial expansion of the lattice perpendicular to the implanted surface and to change the magnetic anisotropy of metallic multilayers through intermixing of interfaces.[6,18,19] This study thoroughly explores the feasibility of using the damage caused by Ar^+ ion implantation to induce lattice strain and PMA in LSMO films that possess in-plane magnetic anisotropy in the as-deposited (AD) state. The choice of inert Ar^+ ions ensures that doping effects of the Ar^+ ions themselves can be excluded. Ultimately, large *c*/*a*-ratios can be tailored though functional properties degrade as the implantation dose increases above a critical dose. By selecting implantation conditions spanning from those that induce negligible impact on material properties to complete amorphization of the crystalline order, the capabilities of this fabrication method can be properly assessed.

30 nm thick LSMO films were deposited epitaxially by pulsed laser deposition on (001)-oriented STO, LSAT, and $SrLaGaO_4$ (SLGO) substrates. The substrates were held at 700 °C in 300

© Author(s) 2020

mTorr O_2 during deposition, and the KrF excimer laser density was 1.0 J/cm^2 with a repetition rate of 1 Hz. Ar^+ ion implantation was performed at room temperature at Innovion Corporation (San Jose, CA) with implant doses ranging between 3×10^{12} Ar/cm^2 and 3×10^{15} Ar/cm^2 with 50 keV ions incident at a 7° offset from the sample normal. X-ray diffraction (XRD) and x-ray reflectivity (XRR) were measured using a four-circle Bruker D8 Discover diffractometer to characterize the structural quality of the films. To probe the electronic and magnetic properties, x-ray absorption (XA) and x-ray magnetic circular dichroism (XMCD) spectra were collected at 80 K at beamline 4.0.2 at the Advanced Light Source using total electron yield (TEY) mode. The x rays were incident at a 30° grazing angle relative to the sample surface, and a magnetic field of 0.5 T was applied along the beam direction. Magnetic hysteresis loops were measured using a superconducting quantum interference device (SQUID) magnetometer at 10 K.

The ion-implantation energy was selected based on Stopping and Range of Ions in Matter (SRIM) calculations[20] that predict a damage profile extending throughout the film thickness and a Gaussian profile for the Ar^+ ions centered at ~30 nm from the film surface (supplementary material). As the dose increases from 3×10^{12} Ar/cm^2 to 3×10^{15} Ar/cm^2, the film (002) XRD peak shifts to lower angles relative to the AD film with considerable broadening and decreased intensity [Fig. 1(a)]. In addition, the diffraction feature originating from the film splits up into multiple peaks, most clearly observed at the 1×10^{14} Ar/cm^2 dose. This multi-peak behavior was observed in Cs-implanted YSZ single crystals and is caused by incoherent x rays scattering due to the inhomogeneous strain profile in the implanted portion of the lattice.[15] The implanted LSMO film has a similar inhomogeneous strain profile with the implantation damage reaching into the substrate, causing the additional intensity on the low angle side of the substrate peak (e.g., 1×10^{13} Ar/cm^2 to 3×10^{13} Ar/cm^2 dose). The rms surface roughness determined by fitting XRR curves is below 10 Å for all implant conditions. Reciprocal space maps (RSMs) around the (103) peak (supplementary material) verify that the induced lattice expansion is confined to the *c*-axis of the film as the H-component of the film peak remains aligned to that of the substrate.

A full description of the structural distortions in the implanted films was determined by fitting the ω–2θ scans using the GID_sl dynamical diffraction modeling program.[21] Details of the fitting procedure are in the supplementary material. A comparison of the depth dependence of the *c*-parameter obtained from GID_sl fitting to the SRIM calculations indicates that the vacancy distribution rather than the Ar^+ ion distribution most closely correlates with the lattice expansion resulting from ion implantation. SRIM simulations predict that a majority of the vacancies are oxygen vacancies. Figure 1(b) summarizes the maximum *c*/*a* ratio within the strain profile of the implanted LSMO films grown on different substrates as a function of the implantation dose. At a dose of 1×10^{15} Ar^+/cm^2, the films can be considered amorphous as the ω–2θ scan monotonically decreases due to diffuse scattering on the low angle side of the substrate peak. With increasing dose, the *c*/*a* ratio increases systematically for all substrates. Therefore, ion implantation serves as an effective method to modify the tetragonal distortion of epitaxial films by expanding the *c*-axis lattice parameter by up to several percents. It should be noted, however, that the crystalline quality of the films is degraded by the energetic Ar^+ ions. The impact of the combined effects of lattice expansion and the change in crystallinity on the functional properties was explored further using a range of experimental techniques.

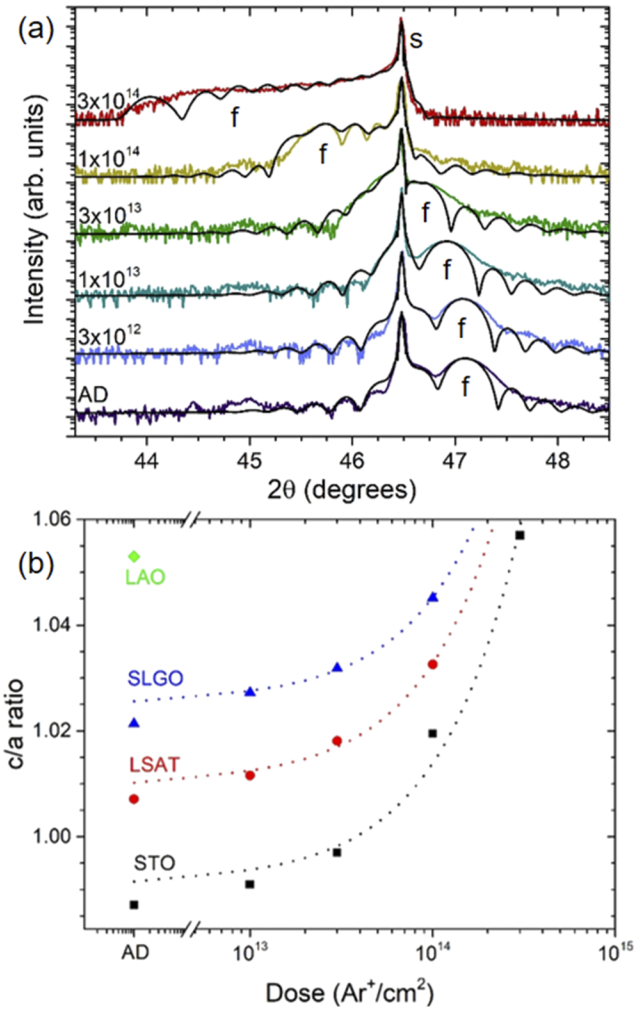

FIG. 1. (a) (002) Experimental ω–2θ scans (colored lines) and GID_sl fits (black lines) for implanted LSMO films on STO substrates. Labels correspond to the implantation dose in Ar/cm^2. Film and substrate peaks are denoted with "f" and "s," respectively. (b) Maximum *c*/*a* ratio for LSMO films on different substrates as a function of the implantation dose. Dotted lines are guides for the eye.

XA measurements involve excitation of electrons from 2*p* core levels to unoccupied 3*d* states in the valence band and are sensitive to the chemical environment of the ion being probed. Furthermore, the absorption of circularly polarized x rays depends on the orientation of magnetic moments, and XMCD spectra can be defined as the difference in XA spectra acquired with the x-ray helicity parallel/antiparallel to the sample magnetization.[22,23] In TEY mode, the XA/XMCD spectra probe the top 5–10 nm of the films rather than the full film thickness.[24] Figure 2 shows Mn-XA/XMCD spectra for the implanted LSMO films grown on STO substrates. The observed trends are consistent for implanted films deposited on LSAT and

© Author(s) 2020

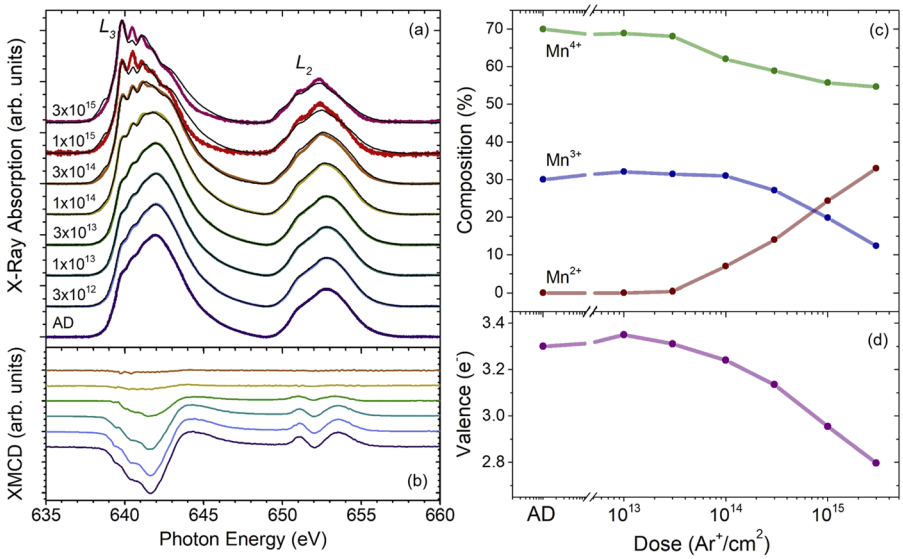

FIG. 2. (a) XA and (b) XMCD spectra for implanted LSMO films on STO substrates. Colored and black lines represent experimental data and fits from a linear combination of reference spectra, respectively. (c) Mn cation populations and (d) calculated formal Mn valence as a function of the implantation dose.

SLGO substrates, but the following XA analysis is focused on STO samples for clarity. The AD film shows the expected XA/XMCD spectral shape for LSMO with mixed Mn^{3+}/Mn^{4+} ions, which leads to robust magnetic properties through the double exchange mechanism.[25,26] The XA/XMCD spectral shapes remain unchanged as the dose increases to a critical dose of 3×10^{13} Ar/cm^2 above which additional features begin to emerge at the low energy side of the L_3 peak, indicating changes in the average Mn valence state. The XA spectra can be described using a linear combination of reference spectra for octahedrally coordinated Mn ions with different valence states, and the weight of each is used to estimate the average Mn valence state. For fitting, MnO (Mn^{2+}), Mn_2O_3 (Mn^{3+}), and Li_2MnO_3 (Mn^{4+}) spectra (supplementary material [27]) were combined with the AD XA spectrum with a nominal valence state of 70% Mn^{4+}/30% Mn^{3+} ions based on the Sr/La ratio. Black lines in Fig. 2(a) represent best fits to the XA spectra, and the results of this analysis are presented in Fig. 2(c). Above the critical dose of 3×10^{13} Ar/cm^2, the concentration of Mn^{2+} ions rises rapidly with increasing dose, replacing both Mn^{3+} and Mn^{4+} ions at equal rates, leading to a decrease in the average Mn valence state. At the highest implantation dose, 3×10^{15} Ar/cm^2, Mn^{2+} and Mn^{4+} ions constitute nearly 90% of the Mn ions with an average valence of $Mn^{2.8+}$. In order to maintain charge neutrality in the LSMO film, this reduced valence state translates to an oxygen stoichiometry of $La_{0.7}Sr_{0.3}MnO_{2.75}$.

The fact that the Mn XMCD spectral shape remains unchanged below a critical dose of 3×10^{13} Ar/cm^2 signifies that the Mn^{3+}–Mn^{4+} double exchange mechanism continues to be the dominant source of magnetism and that no appreciable change in the ratio of spin to orbital moments takes place. Furthermore, no indication of XMCD associated with Mn^{2+} ions was detected at any dose. SQUID hysteresis loops (supplementary material) performed with the magnetic field applied in the film plane demonstrate that the sample-averaged magnetic properties mirror those of the sample surface probed by the XMCD measurement. As the dose increases, saturation magnetization (M_S) and Curie temperature decrease, while coercivity increases. For doses above 1×10^{14} Ar/cm^2, the LSMO films continue to show hysteresis at 10 K, but the M_S value is only 2%–10% of the AD LSMO film, indicating that little magnetic order persists. These trends are consistent with a ferromagnetic oxide that becomes more structurally disordered from Ar^+ ion implantation and with an increased concentration of oxygen vacancies.[28–32]

The magnetic anisotropy of the LSMO films as a function of the c/a ratio was investigated by measuring the in-plane and out-of-plane magnetic hysteresis loops for films grown on STO, LSAT, and SLGO substrates (Fig. 3). Films implanted with a dose of 3×10^{13} Ar/cm^2 were chosen as a balance between a sizable magnitude of lattice expansion (~1%) while maintaining M_S values >100 emu/cm^3. The AD LSMO film on the STO substrate shows a strong in-plane anisotropy that is characterized by a square hysteresis loop with large in-plane remanent magnetization, M_R, and a large effective magnetic anisotropy constant, $K_{eff} \sim -1.7 \pm 0.1 \times 10^6$ erg/cm^3 for the out-of-plane hysteresis loop. As the c/a ratio increases, by changing either the substrate type or ion implantation, the LSMO films become more isotropic, i.e., M_R for the in-plane hysteresis loop decreases, and K_{eff} decreases for the out-of-plane hysteresis loop. All samples demonstrate clear modification of the magnetic anisotropy by ion implantation, approaching PMA for the implanted films on LSAT and SLGO substrates with $K_{eff} \sim +1.3 \pm 0.4 \times 10^5$ and $-7 \pm 6 \times 10^4$ erg/cm^3, respectively. It should be noted that K_{eff} values take into account the combined contributions of the reduced M_S values and a decrease in the impact of the ion implantation process on magnetic anisotropy.

The compilation of structural, electronic, and magnetic characterizations of the ion-implanted LSMO films suggests a transition in the type of damage imposed by the ion-implantation process with a critical dose of 3×10^{13} Ar^+/cm^2. Previous work on implantation of noble gas ions into silicon indicated that a transition from elastic to plastic deformation occurred at a critical implant dose.[33] For Ar^+ ions implanted into Si, this critical dose was 1×10^{14} Ar/cm^2

© Author(s) 2020

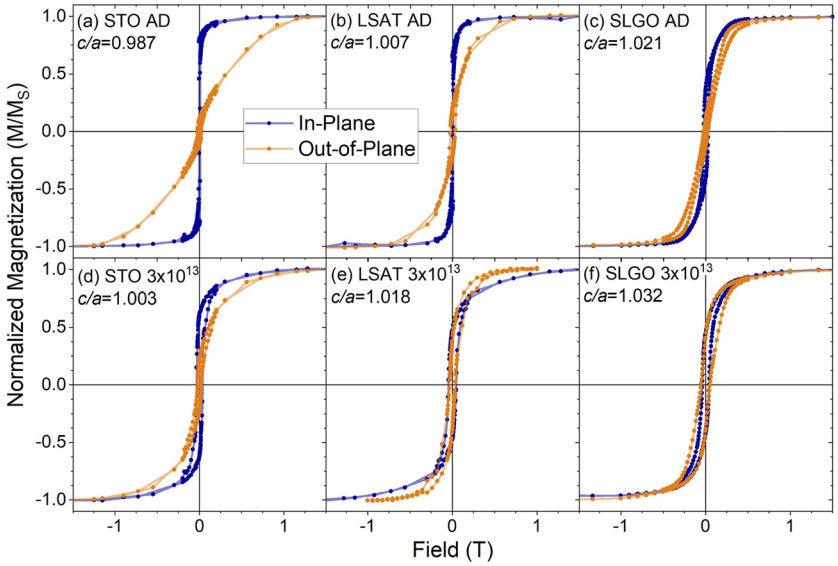

FIG. 3. Normalized hysteresis loops for AD and 3 × 10^{13} Ar/cm^2 implanted films on [(a) and (d)] STO, [(b) and (e)] LSAT, and [(c) and (f)] SLGO substrates, respectively.

and it decreased as the mass of the noble gas element increased. In the elastic regime for LSMO films (dose ≤3 × 10^{13} Ar^+/cm^2), the average Mn valence state remains unchanged and the double exchange mechanism remains responsible for the magnetic properties without a significant change in the ratio of spin to orbital moments. Therefore, the main contribution to the change in magnetic anisotropy toward PMA results from the change in the *c*/*a* ratio. As the *c*/*a* ratio increases with increasing implant dose, the overlap between the Mn 3*d* and O 2*p* orbitals decreases, leading to a suppression of M_S, while defects from the ion-implantation process cause pinning of domain walls and an increase in coercivity. This result can be explained by a preferential filling of Mn $3d_{3z^2-r^2}$ orbitals that are stabilized by reduced Coulomb interactions with O 2*p* orbitals along the increased *c*-axis. The proposed mechanism for PMA in compressively strained manganites and cobaltites with the *c*/*a* ratio >1 involves a bulk magnetostriction effect due to the positive (negative) sign of the longitudinal (transverse) magnetostriction coefficients, respectively.[13,34,35] In the plastic regime, the crystalline quality rapidly degrades that is accompanied by a decrease in the average Mn valence state and an increase in the concentration of oxygen vacancies,[36] and ultimately in a loss of magnetic properties.

The ability to change the magnetic anisotropy of the LSMO film based on ion implantation opens the possibility to fabricate artificial magnetic skyrmions and other non-trivial spin textures that require adjacent regions of differing magnetic anisotropy within a single layer of material.[4–8] A process such as that developed by Takamura *et al.*[37,38] could fabricate structures with in-plane anisotropy defined by a mask pattern, and a subsequent flood ion implantation would define surrounding regions with PMA or non-magnetic properties. The necessary implant conditions can be determined using SRIM simulations since, as discussed above, lattice expansion is most closely correlated with the oxygen vacancy distribution induced by ion implantation. In contrast to prior studies where oxygen vacancies have been introduced by vacuum annealing,[29–32] the ion implantation-based technique can tailor the local *c*/*a* ratio and distribution of oxygen vacancies based on the implant conditions and mask design, rather than relying on the isotropic diffusion of oxygen ions.

This study comprehensively investigated the variation of magnetic, electronic, and structural properties of Ar^+ ion-implanted LSMO thin films and explored the potential to create PMA through a uniaxial expansion along the *c*-axis. As the dose increases, two distinctive regimes were identified corresponding to elastic and plastic deformation. In the elastic regime, the double exchange mechanism between Mn^{3+}/Mn^{4+} ions is preserved, while the increase in the *c*/*a* ratio favors an out-of-plane magnetic anisotropy, whereas the plastic regime is characterized by significant crystalline damage, a decreased average Mn valence state, and the near-complete suppression of ferromagnetic properties. RSMs confirm that the lattice expansion is confined to the *c*-axis, as the film remains coherently strained for doses up to 1 × 10^{15} Ar^+/cm^2. This ability to locally tune the magnetic properties of complex oxides enables the fabrication of magnetic spin textures, consisting of adjacent regions of differing magnetic anisotropy within a single thin film.

See the supplementary material for RSMs, GID_sl dynamical diffraction modeling, reference XA spectra, SRIM calculations, and SQUID measurements.

Funding for these experiments was obtained from the National Science Foundation (Grant Nos. DMR 1411250 and 1745450). This research used resources of the Advanced Light Source, which is a Department of Energy Office of Science User Facility, under Contract No. DE-AC02-05CH11231.

REFERENCES

[1] S. N. Piramanayagam, J. Appl. Phys. **102**(1), 011301 (2007).
[2] A. Fert, N. Reyren, and V. Cros, Nat. Rev. Mater. **2**, 17031 (2017).

© Author(s) 2020

[3]K. Everschor-Sitte, J. Masell, R. M. Reeve, and M. Kläui, J. Appl. Phys. **124**(24), 240901 (2018).
[4]J. Li, A. Tan, K. W. Moon, A. Doran, M. A. Marcus, A. T. Young, E. Arenholz, S. Ma, R. F. Yang, C. Hwang, and Z. Q. Qiu, Nat. Commun. **5**, 4704 (2014).
[5]D. A. Gilbert, B. B. Maranville, A. L. Balk, B. J. Kirby, P. Fischer, D. T. Pierce, J. Unguris, J. A. Borchers, and K. Liu, Nat. Commun. **6**, 8462 (2015).
[6]S. Zhang, A. K. Pedford-Long, and C. Phatak, Sci. Rep. **6**, 31248 (2016).
[7]B. F. Miao, L. Sun, Y. W. Wu, X. D. Tao, X. Xiong, Y. Wen, R. X. Cao, P. Wang, D. Wu, Q. F. Zhan, B. You, J. Du, R. W. Li, and H. F. Ding, Phys. Rev. B **90**(17), 174411 (2014).
[8]L. Sun, R. X. Cao, B. F. Miao, Z. Feng, B. You, D. Wu, W. Zhang, A. Hu, and H. F. Ding, Phys. Rev. Lett. **110**(16), 167201 (2013).
[9]T. M. Perekalina, I. E. Lipin'ski, V. A. Timofeeva, and S. A. Cherkezyan, Fiz. Tverd. Tela **32**(10), 3146–3148 (1990).
[10]D. Yi, C. L. Flint, P. P. Balakrishnan, K. Mahalingam, B. Urwin, A. Vailionis, A. T. N'Diaye, P. Shafer, E. Arenholz, Y. Choi, K. H. Stone, J.-H. Chu, B. M. Howe, J. Liu, I. R. Fisher, and Y. Suzuki, Phys. Rev. Lett. **119**(7), 077201 (2017).
[11]Y. Suzuki, H. Y. Hwang, S.-W. Cheong, and R. B. van Dover, Appl. Phys. Lett. **71**(1), 140–142 (1997).
[12]F. Tsui, M. C. Smoak, T. K. Nath, and C. B. Eom, Appl. Phys. Lett. **76**(17), 2421–2423 (2000).
[13]J. Walter, S. Bose, M. Cabero, G. Yu, M. Greven, M. Varela, and C. Leighton, Phys. Rev. Mater. **2**(11), 111404 (2018).
[14]O. W. Holland, J. D. Budai, and C. W. White, Appl. Phys. Lett. **57**(3), 243–245 (1990).
[15]A. Debelle and A. Declémy, Nucl. Instrum. Methods Phys. Res., Sect. B **268**(9), 1460–1465 (2010).
[16]H. Guo, S. Dong, P. D. Rack, J. D. Budai, C. Beekman, Z. Gai, W. Siemons, C. M. Gonzalez, R. Timilsina, A. T. Wong, A. Herklotz, P. C. Snijders, E. Dagotto, and T. Z. Ward, Phys. Rev. Lett. **114**(25), 256801 (2015).
[17]A. Herklotz, Z. Gai, Y. Sharma, A. Huon, S. F. Rus, L. Sun, J. Shen, P. D. Rack, and T. Z. Ward, Adv. Sci. **5**(11), 1800356 (2018).
[18]C. Chappert, H. Bernas, J. Ferré, V. Kottler, J.-P. Jamet, Y. Chen, E. Cambril, T. Devolder, F. Rousseaux, V. Mathet, and H. Launois, Science **280**(5371), 1919–1922 (1998).
[19]J. Fassbender and J. McCord, J. Magn. Magn. Mater. **320**, 579–596 (2008).
[20]J. F. Ziegler, M. D. Ziegler, and J. P. Biersack, Nucl. Instrum. Methods Phys. Res., Sect. B **268**, 1818–1823 (2010).
[21]S. Stepanov and R. Forrest, J. Appl. Crystallogr. **41**(5), 958–962 (2008).
[22]C. T. Chen, F. Sette, Y. Ma, and S. Modesti, Phys. Rev. B **42**(11), 7262–7265 (1990).
[23]G. van der Laan and A. I. Figueroa, Coord. Chem. Rev. **277-278**, 95–129 (2014).
[24]J. S. Lee, D. A. Arena, P. Yu, C. S. Nelson, R. Fan, C. J. Knane, S. Langridge, M. D. Rossel, R. Ramesh, and C.-C. Kao, Phys. Rev. Lett. **105**, 257204 (2010).
[25]P. W. Anderson and H. Hasegawa, Phys. Rev. **100**, 675–681 (1955).
[26]C. Zener, Phys. Rev. **82**, 403–405 (1951).
[27]R. Qiao, Y. Wang, P. Olalde-Velasco, H. Li, Y.-S. Hu, and W. Yang, J. Power Sources **273**, 1120–1126 (2015).
[28]V. M. Browning, R. M. Stroud, W. W. Fuller-Mora, J. M. Byers, M. S. Osofsky, D. L. Knies, K. S. Grabowski, D. Koller, J. Kim, D. B. Chrisey, and J. S. Horwitz, J. Appl. Phys. **83**(11), 7070–7072 (1998).
[29]K. M. Krishnan and H. L. Ju, Phys. Rev. B **60**(21), 14793–14803 (1999).
[30]H. L. Ju, J. Gopalakrishnan, J. L. Peng, Q. Li, G. C. Xiong, T. Venkatesan, and R. L. Greene, Phys. Rev. B **51**(9), 6143–6146 (1995).
[31]J.-M. Liu, Q. Huang, J. Li, C. K. Ong, Z. C. Wu, Z. G. Liu, and Y. W. Du, Phys. Rev. B **62**(13), 8976–8982 (2000).
[32]Y. Meng, W. He, A. Li, G. Li, and S. Jin, Physica B **407**, 2416–2420 (2012).
[33]E. P. EerNisse, Appl. Phys. Lett. **18**(12), 581–583 (1971).
[34]C. Kwon, M. C. Robson, K.-C. Kim, J. Y. Gu, S. E. Lofland, S. M. Bhagat, Z. Trajanovic, M. Rajeswari, T. Venkatesan, A. R. Kratz, R. D. Gomez, and R. Ramesh, J. Magn. Magn. Mater. **172**(3), 229–236 (1997).
[35]G. Srinivasan, E. T. Rasmussen, B. J. Levin, and R. Hayes, Phys. Rev. B **65**, 134402 (2002).
[36]Y. M. Baikov, E. I. Nikulin, B. T. Melekh, and V. M. Egorov, Phys. Solid State **46**(11), 2086–2093 (2004).
[37]Y. Takamura, R. V. Chopdekar, A. Scholl, A. Doran, J. A. Liddle, B. Harteneck, and Y. Suzuki, Nano Lett. **6**(6), 1287–1291 (2006).
[38]E. Folven, Y. Takamura, and J. K. Grepstad, J. Electron Spectrosc. Relat. Phenom. **185**, 381–388 (2012).

© Author(s) 2020